Electrical Properties of Yttria-Stabilized Zirconia, YSZ Single Crystal: Local AC and Long Range DC Conduction

Xavier Vendrell *,z and **Anthony R. West** *

Department of Materials Science and Engineering, University of Sheffield, Sheffield S1 3JD, United Kingdom

Widely-used complex plane analysis of impedance data is insufficiently sensitive to characterize fully the bulk properties of YSZ single crystal. Instead, more extensive data analysis is needed which uses a combination of parallel, admittance-based formalisms and series, impedance-based formalisms. Bulk electrical properties are measured at higher frequencies and contain contributions from both long range conduction and local dielectric relaxation. At lower frequencies, electrode–sample contact impedances are measured and are included in full equivalent circuit analysis. The impedance of YSZ crystal of composition 8 mol% Y_2O_3 in the (110) orientation, with Pt electrodes, was measured over the temperature range 150–750°C and frequency range 0.01 Hz-3 MHz. Full data analysis required (i) a parallel constant phase element (CPE)–resistance (R) combination to model the electrode response, (ii) a series R-C element to represent local reorientation of defect dipoles and (iii) a R-C-CPE element to represent long range oxide-ion conduction; (ii) and (iii) together model the bulk response. The dielectric element underpins all discussions about defect structure and properties of YSZ but has not been included previously in analysis of impedance data. The new equivalent circuit that is proposed should allow better separation of bulk and grain boundary impedances of YSZ ceramics.
 [DOI: 10.1149/2.0881811jes]

Manuscript submitted June 28, 2018; revised manuscript received August 15, 2018. Published August 25, 2018.

Yttria-stabilized zirconia (YSZ) is a very well-known oxide ion conductor that is used as the solid electrolyte in solid oxide fuel cells and oxygen gas sensors.[1–3] It usually takes the form of a high-density ceramic in which the bulk resistance in series with a grain boundary resistance gives the overall sample resistance.[4] In almost all cases, the grain boundary resistance is present and cannot be eliminated readily by attention to ceramic processing conditions. The nature of the grain boundary impedance is often unclear, although significant compositional differences from the bulk, associated with dopant segregation, may be involved.[5,6]

In order to measure sample impedances, sample-electrode contacts are necessary and therefore, appropriate consideration of their associated impedances forms part of the overall impedance analysis. For YSZ, contact impedances include contributions from the blocking of oxide ions at the sample-electrode interface, charge transfer resistances associated with the O^{2-}/O_2 redox couple and the diffusion of O_2 molecules between the surrounding atmosphere and the sample-electrode interface. Usually, electrode contact impedances are well-separated on a frequency scale from bulk/grain boundary impedances because they have much higher associated capacitances, C: typically $(1–10) \times 10^{-6}$ F for the electrode contact compared with $\sim 1 \times 10^{-10}$ F for a grain boundary capacitance and $(2–3) \times 10^{-12}$ F for a bulk capacitance. Relaxation frequencies, ω, are given ideally by $\omega\tau = 1$, where $\tau = RC$ and therefore, the frequency maxima of impedance semicircles, arcs or peaks associated with bulk/grain boundary impedances are usually separated by several decades from those of electrode-sample contact impedances. This allows the visualization and characterization of sample properties without the necessity to eliminate sample-electrode contact impedances but, of course, a full analysis of properties, including the modelling of sample-electrode impedances, can also be carried out, as shown here.

Conductivity Arrhenius plots for oxide ion conduction in YSZ have been reported on many occasions and we do not give a comprehensive survey of the early literature here. Many data sets, especially for compositions that exhibit high oxide ion conductivity, show distinct curvature of the Arrhenius plots which is attributed to the trapping at lower temperatures of mobile oxide ion vacancies in vacancy-dopant defect complexes.[3,7–10] Two possible defect complexes that are widely discussed are the charged dimer, $(Y'_{Zr}V_O^{\bullet\bullet})^{\bullet}$ and the neutral trimer, $(Y'_{Zr}V_O^{\bullet\bullet}Y'_{Zr})^{x}$ and their relative proportion may change with composition. Typical reported activation energies are ca 1.1 eV at low temperatures and ca 0.85 eV at high temperatures; the difference of ca 0.25 eV is often regarded as the dissociation enthalpy of the defect complexes.[11–15]

It is standard practice in the analysis of impedance data of YSZ ceramics and single crystals to present data in the form of impedance complex plane plots, Z''/Z' and to obtain bulk conductivity data from the low frequency intercept of the high frequency arc or (distorted) semicircle on the real, Z' axis; sometimes, the data are fitted to a semicircle whose center is depressed below the Z' axis.[16,17] Impedance complex plane, Z*, plots represent a good method to separate bulk and grain boundary resistances since the appropriate equivalent circuit for data analysis is a series combination of the parallel RC elements that represent the bulk and grain boundary components. However, Z* plots on linear scales give undue weighting to the largest resistances in a sample and effectively, exclude from view any low resistance components such as those associated with inhomogeneous ceramics that may have conductive grain cores but resistive grain boundaries.

A more comprehensive analysis of impedance data that avoids such weighting is obtained by presenting the same impedance data in at least two of the four formalisms**:** impedance Z^*, admittance Y^*, permittivity ε^* and electric modulus M^* using the following interconversions:[18,19]

$$Z^* = (Y^*)^{-1} \quad [1]$$

$$M^* = j\omega C_0 Z^* \quad [2]$$

$$\varepsilon^* = (M^*)^{-1} \quad [3]$$

where C_0 is the vacuum capacitance of the conductivity cell, without a sample in place. Each of these formalisms has real and imaginary components, such as:

$$Z^* = Z' - jZ'' \quad [4]$$

Following these interconversions, data may be plotted as either complex plane (or Nyquist) plots, e.g. $Z''vs\ Z'$ or as spectroscopic (or Bode) plots, e.g. Z'', $M''vs \log f$.

It was shown recently that accurate fitting of impedance data of YSZ ceramics to the traditional equivalent circuit consisting of a series combination of bulk and grain boundary impedances was not entirely successful. Instead, better agreement was obtained on introduction of an additional series RC element, that was attributed to a localized dipolar reorientation process, into the equivalent circuit;[20] this element was placed in parallel with the element representing long range *dc* conduction through the sample.

*Electrochemical Society Member.
zE-mail: x.vendrell@sheffield.ac.uk

The objectives of the present work were to (1) obtain impedance data on a YSZ single crystal that therefore, did not contain any grain boundary contribution, (2) find the most appropriate equivalent circuit to model the bulk impedance data by considering the possibility of a parallel combination of both long range and local conduction processes, (3) extract values for the various circuit parameters as a function of temperature and (4) model and characterize the impedance response of the sample-electrode interface.

Experimental

Single crystals of yttria-stabilized zirconia of composition 8 mol% Y_2O_3 (8YSZ) were obtained from Pi-Kem. The crystals were provided as plates parallel to lattice planes of the set {110} with dimensions 5 × 5 × 0.5 mm. The crystals were already polished on a pair of opposite plate faces and were used as-received. Electrodes were fabricated from Pt-paste on opposite plate faces which was dried and hardened by heating at 900°C for 2 h. The crystals were then attached to the Pt leads of a conductivity jig which was placed inside a horizontal tube furnace.

Impedance measurements in air were obtained over the temperature range 150 to 750°C and recorded using two instruments, an Agilent 4294A over the frequency range 40 Hz to 3 MHz and a Solartron 1260A over the frequency range 0.01 Hz to 1 MHz. Most of the data were collected using the Agilent, but use of the Solartron enabled an extra three decades at low frequency to be accessed, especially for measurements at high temperatures; the nominal ac voltage used was 100 mV. At each temperature, the system was allowed to equilibrate for 1 h, without voltage applied, prior to impedance measurements. Data were analyzed using Zview (Scribner Associates Inc.) software. Impedance data were corrected for crystal geometry and electrode contact area; this allowed resistance and capacitance to be reported in resistivity and permittivity units of Ω cm and F cm^{-1}, respectively. Open circuit measurements of an empty jig were used to obtain the blank parallel capacitance, C_0, of the jig and leads, which was subtracted from the values obtained with a sample present in the jig. In order to obtain the C_0 value, the jig was assembled with hardened Pt electrodes of similar dimension, but without a sample in place. Closed circuit measurements were obtained by connecting the two electrodes directly and used to correct for the series jig resistance.

The first objective in data analysis was to find the most appropriate equivalent circuit to represent data sets; to achieve this, data were presented in various formats so as to visually, gain an overview of the various components shown by the data. We found the following presentations to be particularly appropriate and were the ones used here.

First, $Z''vs\ Z'$ plots served to highlight the main resistive components but had the disadvantage that small additional resistances were effectively hidden. As also shown later, $Z''vs\ Z'$ plots were not a good discriminator between the possible equivalent circuits.

Second, $\log Y' vs \log f$ plots gave equal weighting to the various conducting elements and in particular, highlighted the presence of a high frequency dispersion which was modelled using the bulk constant phase element, CPE.

Third, combined $Z''/M''vs \log f$ plots were examined to see whether the main resistance, shown by the largest arc in plots of $Z''vs\ Z'$ or the largest peak in plots of $Z''vs \log f$, represented the sample bulk. If it did, the Z'' peak should coincide approximately with the largest peak in $M''vs \log f$ which corresponds to the bulk response since it represents the element with the smallest (ie bulk) capacitance.

Fourth, $\log C'vs \log f$ [$C' \equiv \varepsilon' C_0$] plots were examined since they gave equal weighting across the frequency spectrum to the various capacitive elements, including the limiting high frequency capacitance, any intermediate frequency capacitances and low frequency, electrode-sample contact capacitances.

The second objective in data analysis was to fit the experimental data to possible equivalent circuits. It is essential to identify the most appropriate equivalent circuit in order to have correct equations to evaluate the component R, C and CPE parameters. Fit quality and accuracy were assessed by both visual inspection of the data in various formalisms, as indicated above and the residuals between experimental and fitted data.

The third objective was to determine the dependence of the various circuit component values on temperature and interpret the component parameters in terms of sample characteristics.

Results and Discussion

Impedance data are shown for the (110) orientation in Figure 1 as (a) a Z^* complex plane plot and (b) Y', (c) M''/Z'', and (d) C' spectroscopic plots at one representative temperature, 306°C.

At this temperature, data are dominated by the sample response whereas sample-electrode contact impedances start to appear in the data at higher frequencies. The Z^* data (a) show a slightly distorted high frequency arc with a low frequency inclined spike (inset). The initial interpretations of these data are as follows:

Using conventional complex plane analysis, the high frequency arc (a) can be fitted to an appropriate function and the dc resistance value of the sample obtained from the low frequency intercept on the Z' axis. The capacitance associated with sample resistance can be obtained from the arc maximum using the relation:

$$\omega RC = 1 \qquad [5]$$

As expected for a single crystal, there is no additional arc at lower frequencies associated with a grain boundary impedance. The low frequency spike represents the onset of the sample-electrode contact impedance.

On presenting the data in other formats (b-d), additional features are seen. Y' data (b) show a low frequency plateau corresponding to the dc conductivity, that is also obtained from the Z''/Z' plots, and in addition, a high frequency, power law dispersion. Such dispersions are a characteristic feature of all ionically-conducting materials (and probably, many semiconducting materials as well) and are a manifestation of Jonscher's Universal Dielectric Response.[21] The dispersions correspond to regions of the frequency/time domain where local conduction processes occur but on shorter timescales than *dc* processes at lower frequencies. With increasing frequency in the dispersion region, increasingly easier conduction processes are detected and the measured *ac* conductivity rises.

Over the years, various empirical functions had been used to model the dispersion region until the seminal work of Jonscher who recognized the universal occurrence of a power law dependence of *ac* conductivity on frequency. Most recently, Almond and co-workers demonstrated that such power law dependence is a natural consequence of an equivalent circuit that consists of a large resistor-capacitor network.[22,23] Until their demonstration, the significance of the characteristic slope, *n*, of the log conductivity-log frequency plots was not well appreciated but is now regarded simply as the ratio between the numbers of capacitive and resistive connections in the network. This high frequency power law conductivity dispersion is modelled in equivalent circuits by inclusion of a CPE whose admittance takes the form:

$$Y^*_{CPE} = Y_0(j\omega)^n = Y_0\omega^n\,[cos\,(n\pi/2) + \ jsin\,(n\pi/2)] = A\omega^n + jB\omega^n \qquad [6]$$

The bulk electrical properties of many ionic conductors are modelled well by an equivalent circuit A, Figure 2, that consists of a parallel combination of a resistance, R, which represents the *dc* conductivity, a capacitance, C which represents the limiting high frequency permittivity, often given the symbol ε_∞ and a CPE which represents the power law dispersion.

M''/Z'' plots, Figure 1c show one main peak in each spectrum with the peak maximum at slightly higher frequency for M'' than for Z''. The peak maximum of an ideal, Debye-like M'' peak is inversely proportional to the capacitance of the R-C element responsible for the

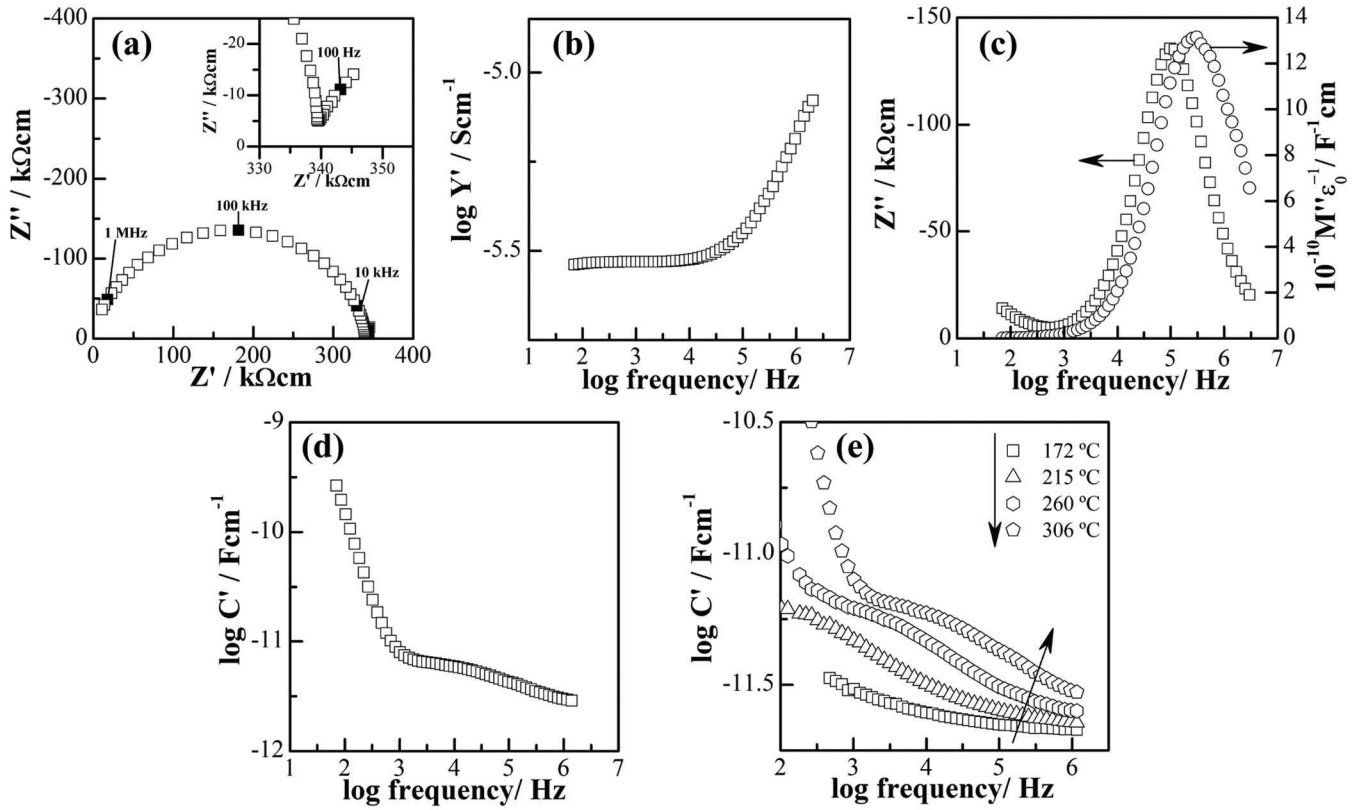

Figure 1. Impedance spectra for 8YSZ single crystal with the field perpendicular to (110) measured at 306°C. (a) Experimental data shown for impedance complex plane plot; the frequencies of some data points are indicated, (b) Y' spectroscopic plot, (c) Z''/M'' spectroscopic plots, (d) C' spectroscopic plot and (e) C' data at several temperatures.

peak:

$$M''_{max} = C_0/2C \quad [7]$$

where C_0 is the capacitance of the empty jig that contains electrodes in the same geometrical arrangement. Since the smallest capacitance in an equivalent circuit usually represents the bulk component, the M'' peak, and the associated Z'' peak, enable assignment of these peaks to the bulk sample conductivity. The observed small separation in peak maximum frequencies (c) is a direct consequence of the presence of the CPE in the equivalent circuit A, Figure 2. In addition, the CPE causes the M'', Z'' peaks to broaden asymmetrically: the M'' peak is Debye-like at frequencies lower than the peak maximum but broadened at higher frequencies whereas, the Z'' peak is Debye-like at frequencies above the peak maximum but broadened at lower frequencies.[24]

C' data, Figure 1d, show two dispersions at high and low frequency with some evidence for both a limiting high frequency plateau at ~2 pFcm^{-1} and a poorly-resolved intermediate frequency plateau at ~6 pFcm^{-1}. The high frequency plateau in C' corresponds to a permittivity, of ~25, using:

$$\varepsilon' = C/e_0 \quad [8]$$

where e_0 is the permittivity of free space, 8.854×10^{-14} Fcm^{-1}. This ε' value is attributed to the bulk permittivity, ε_∞ of the crystal. C' data at lower temperatures show this plateau more clearly, Figure 1e.

The intermediate frequency plateau has an effective permittivity of ~70. It is not immediately obvious how this should be assigned since data obtained from single crystals should be free from any grain boundary or surface layer impedances and anyway, such a capacitance value of ~6 pFcm^{-1} would represent a significant volume fraction of the sample and be much smaller than expected for a grain boundary or surface layer.[19] It therefore, seems likely to represent an additional parallel element in the equivalent circuit.

The high values reached by the low frequency dispersion in C' Figure 1d and the observed low frequency spike in Z^*, (a), are attributed to blocking capacitance effects at the crystal-electrode interface and in particular, are associated with oxide-ion conduction of the YSZ crystal.[25]

Further interpretation of the impedance data required fitting to possible equivalent circuits, to establish the most appropriate circuit. The assessments of the validity of the possible equivalent circuits were carried out in various ways: (1) by visual comparison of fitted and experimental data over the whole frequency range, using data

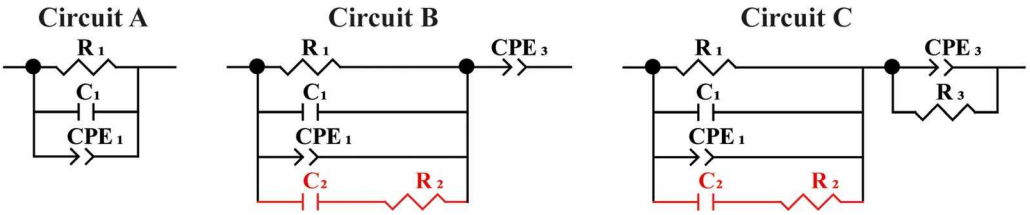

Figure 2. Different equivalent circuits used to model impedance data.

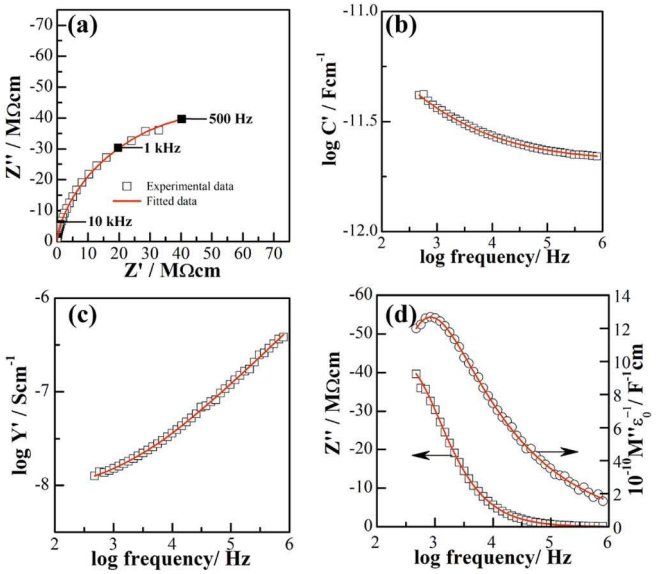

Figure 3. Impedance spectra for 8YSZ single crystal with the field perpendicular to (110) measured at 190°C. (a) Experimental and fitted data to circuit A for impedance complex plane; the frequencies of some data points are indicated, (b) C' spectroscopic plot, (c) Y' spectroscopic plot and (d) Z''/M'' spectroscopic plots.

presentation in different impedance formalisms; (2) from residuals of the fits; (3) by inspection of the fitted parameter values and assignment of the parameters to electrical property characteristics of the sample.

Although impedance data covering 8 decades of frequency were obtained, this was insufficient to fully fit to a complete equivalent circuit at any single temperature. Consequently, partial circuits were used for three temperature ranges: (i) low, (ii) intermediate and (iii) high which were then combined at the end of the analysis to give a master circuit. Finally, at the highest temperatures, (iv), modification to the circuit was required to include the introduction of instrumentation-related inductive effects.

(i) Low temperature data, 170 to 220°C

The first step to establish the most appropriate equivalent circuit was to find a partial circuit that fitted the lowest temperature data sets since, at these temperatures, only the bulk response was detected over the measuring frequency range. The partial circuit A shown in Figure 2 covers the high frequency data associated with the bulk response and includes both *dc* conduction and *ac* conductivities associated with short range, power law effects.[21,26] An excellent fit of low temperature data to this partial circuit was obtained, as shown at 190°C in Figure 3.

The presence of a CPE in the equivalent circuit was readily apparent in two ways. First, as shown in $\log Y' vs \log f$, the CPE represents the power law dispersion, at high frequencies, with slope n, Figure 3c. Second, in plots of $\log C' vs \log f$, the CPE contributes a power law dispersion of slope $(n\text{-}1)$ at lower frequencies because $C' = Y''/\omega = B\omega^{n-1}$; this is seen over the frequency range $\sim 10^4$-10^6 Hz in Figure 1d. In the analysis of high frequency data, it is essential that both CPE_1 and C_1 are included in the equivalent circuit.[27] A CPE alone cannot account for experimental data in which both frequency-independent ε_∞ is detected at high frequencies and frequency-dependent C' at lower frequencies.

Unfortunately, this point is often not recognized in the literature, perhaps because data may not extend to frequencies that are high enough to detect ε_∞ and therefore, equivalent circuits that are used to represent the bulk response may contain only R_1 and CPE_1. An alternative reason may be that data presentation is often limited to the use of $Z'' vs\ Z'$ complex plane plots. These are completely insensitive to the presence of high frequency, power law impedances which occur at frequencies close to the origin of $Z'' vs\ Z'$ plots.

(ii) Intermediate temperature data, 260 to 440°C

The second stage in finding an appropriate equivalent circuit was to consider data obtained at increasingly higher temperatures; additional impedance components became apparent in the lower frequency C' data and required inclusion of additional element(s) in the equivalent circuit. The effect of including various possible additional circuit elements was tested based on two strategies. One was to add a second element in series with the bulk element shown in circuit A, Figure 2. This would represent a second series impedance associated with the single crystal and correspond to an electrical inhomogeneity of some kind. Given the small value of the intermediate frequency capacitance seen in Figures 1d, 1e, this electrical inhomogeneity would correspond to a significant volume fraction of the crystal. The second strategy was to consider an additional impedance in parallel with the bulk conductivity represented by circuit A, Figure 2; in order for this to be detected as a separate element, it should have dielectric character and involve a series R-C combination.

It was found that partial circuit B, Figure 2, containing an additional parallel impedance, gave the best fit to the experimental data at intermediate temperatures. This partial circuit has the logical simplicity of combining, in parallel, a conductive element, R_1-C_1-CPE_1 and a dielectric element represented by the C_2-R_2 series combination. Circuit B also contains a series element CPE_3 to represent the onset of impedances associated with the sample-electrode interface. Fits to experimental data recorded at 306°C, are shown in Figures 4a–4d; the residuals are shown in (e) and are small over the entire frequency range.

The suitability of several other plausible equivalent circuits was tested, as shown in Figure 5 and Table I, circuits (D) to (J). Each of these circuits contains the same element, CPE_3 to represent the onset of the electrode-sample interfacial impedance and, therefore, the circuits differ only in the element(s) that represent the bulk response. The results, Figure 5, show that all of these circuits were unsatisfactory for various reasons, as follows.

Circuits (D) and (E) are simple circuits that have a single conducting element to represent the sample bulk. Circuit (D) has the parallel element R_1-CPE_1 whereas (E) has the parallel element R_1-CPE_1-C_1. Both of these are often used in the literature to represent a bulk conductive response; they are in series with element CPE_3 to represent the sample-electrode interface. Residuals and fits for these circuits are not good.

Circuit (F) is the classic circuit used to represent many ceramics with a series combination of elements such as grains, grain boundaries and surface layers. Poor quality of the fits, of C' in particular, as well as poor residuals, show that this circuit is unsuitable.

Circuits (G), (H), (I) and (J) are other possible circuits that combine conductive and dielectric components although none have the logical consistency of a conducting element R_1-C_1-CPE_1, in parallel with a separate dielectric element R_2-C_2 that is present in circuit A. However, these circuits all gave poorer residuals than circuit (B) as well as an unrealistically high value of C_1 for circuit (I).

(iii) High temperature data, 500 to 600°C

The final step in obtaining a circuit that represents the complete range of impedance data was to fully characterize the sample-electrode contact impedance that is seen with increasing temperature and at lower frequencies. The complete, or master, equivalent circuit that includes partial circuits A and B is shown as circuit C in Figure 2, although at these high temperatures, it was not possible to have a sufficiently wide range of frequencies to include refinement of the parameters, R_2, C_2 and C_1 in data fitting. Element CPE_3, that represents the sample-electrode interface at high temperatures, is modified by the addition

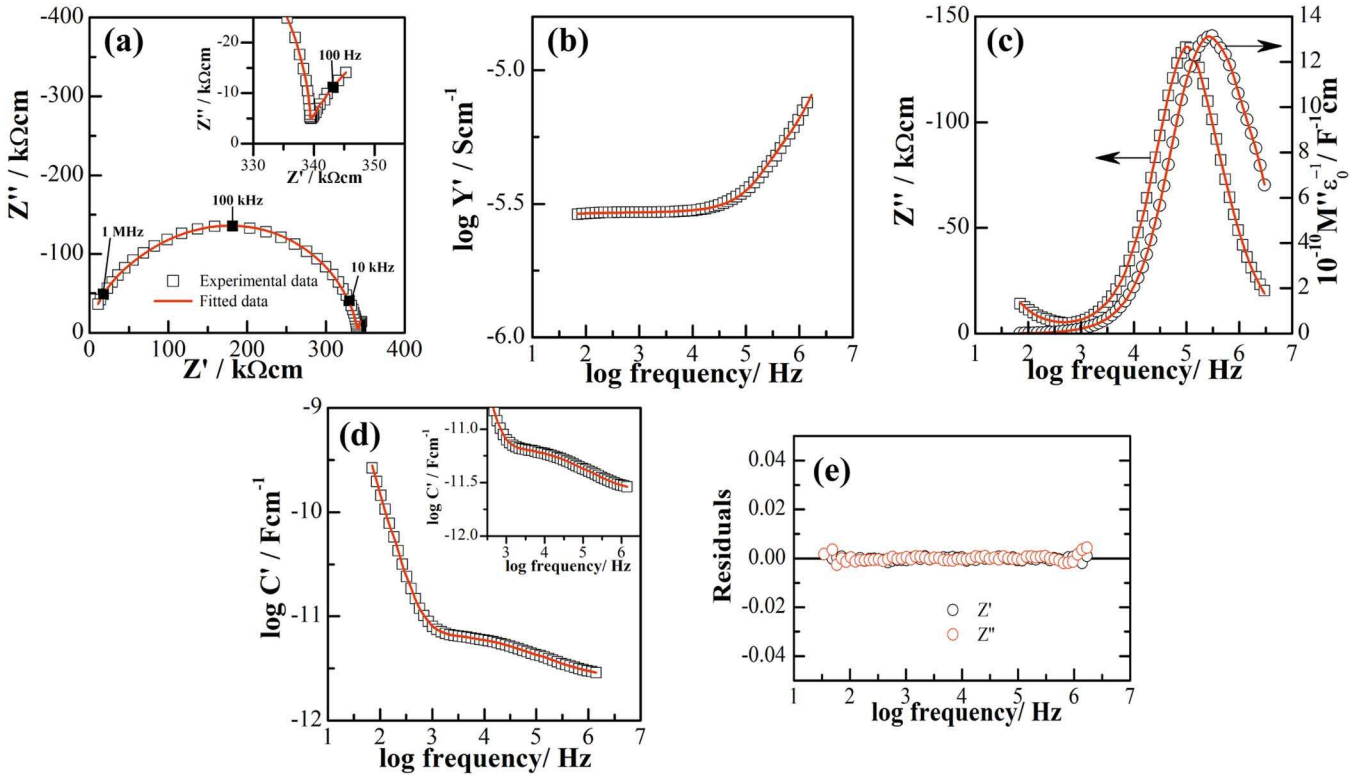

Figure 4. Impedance spectra for 8YSZ single crystal with the field perpendicular to (110) measured at 306°C. (a) Experimental and fitted data to circuit B for impedance complex plane plot; the frequencies of some data points are indicated, (b) Y' spectroscopic plot, (c) C' spectroscopic plot, (d) Z''/M'' spectroscopic plots and (e) residuals.

of a parallel resistance, R_3. Consequently, this interfacial impedance has a finite resistance, as shown by an extrapolated limiting low frequency intercept on the real Z' axis of the impedance complex plane plot, Figure 6a. Since, at high temperatures, data do not extend to frequencies that are high enough to include a significant contribution from elements C_1 and R_2-C_2, circuit C is simplified to give the partial circuit shown in Figure 6a. Fits of Y' and C' spectroscopic plots to this partial circuit are shown in Figures 6b, 6c with residuals in 6d.

(iv) Highest temperature data, 650 to 750°C, with inductive effects

Impedance data at the highest temperatures were similar to those shown in Figure 6, but with one main difference. Instead of the impedance data showing the onset of the R_1-CPE_1 high frequency arc, an inductive effect was seen in which the impedance data at high frequencies cross the Z' axis to give positive values of Z''. This is shown in Figure 7a together with an equivalent circuit containing a series inductance L_1 which gave a good fit to the data at these high temperatures. The effect of the inductance on log Y' at the highest frequencies is shown in (b) and is also seen as a resonance effect in log C' data (c). There was no evidence for an inductive effect in lower temperature data, < 700°C, and therefore the inductance is not included in the master circuit C.

Arrhenius plots for the conductivities σ_1, σ_2 and σ_t obtained from fitting to circuit B are shown in Figures 8a, 8b. The Arrhenius plot for σ_t, (b), is not linear, consistent with that reported for various YSZ samples on many other occasions.[3,7,8,10,28,29] This non-linearity is widely attributed to trapping of oxygen vacancies in vacancy-dopant complexes at low temperatures:[30] at higher temperatures, dissociation of the complexes occurs and the trapping enthalpy is not included in the activation energy. The total conductivity, σ_t, at high temperatures, would therefore represent the hopping of free vacancies.

The temperature dependence of R_3 is shown in Figure 8c and that of the CPE_1 parameters and C_1 is in Figure 8d. Resistance R_3 controls the total *dc* resistance of the sample-electrode arrangement and is associated, in some way, with the sample-electrode-air interface. It also has a very high activation energy, 2.5(1) eV. The two main processes taking place in the vicinity of the interface are redox electron transfer between oxygen species and the diffusion of O_2 molecules through the Pt electrode between the surrounding atmosphere and the sample-electrode interface, both of which could have a significant associated impedance. These processes may be significantly different for the flat, single crystal surfaces used here and the higher surface area, intrinsically rough, surfaces of most YSZ ceramics. Further work is required to better understand the nature of the interface reactions and their effect on resistance R_3.

The Arrhenius plot for σ_1 is parallel to that for σ_t at low temperatures and therefore, has the same activation energy. The similarity of the conductivity data for σ_1 and σ_t at low temperatures is rationalized using the equation for Y* of circuit B. The bulk component of circuit B has four elements in parallel: R_1, C_1, CPE_1 and R_2-C_2 and therefore, its admittance, Y*, can be written as the summation of their individual admittances, as follows:

$$Y^* = \frac{1}{R_1} + j\omega C_1 + (A\omega^n + jB\omega^n) + (R_2 + 1/j\omega C_2)^{-1} \qquad [9]$$

In the low frequency limit, as $\omega \rightarrow 0$, $Y^* = 1/R_1 = \sigma_1 = \sigma_t$ and therefore, σ_t *contains no contribution from the dielectric resistance* R_2. Consequently, R_2 makes no contribution to the intercept values of R_t in impedance complex plane plots and could not be detected by standard impedance complex plane analysis.

The Arrhenius plot for σ_2 has lower activation energy than that for σ_1, and is similar to that of σ_t at high temperatures. σ_2 appears to represent the reorientation of the vacancy-dopant complexes. The interpretation of its lower activation energy would be that dipole reorientation, represented by series element R_2-C_2, does not require dissociation of the complexes; hopping of the oxygen vacancies within the complexes is therefore similar to the hopping of free vacancies at

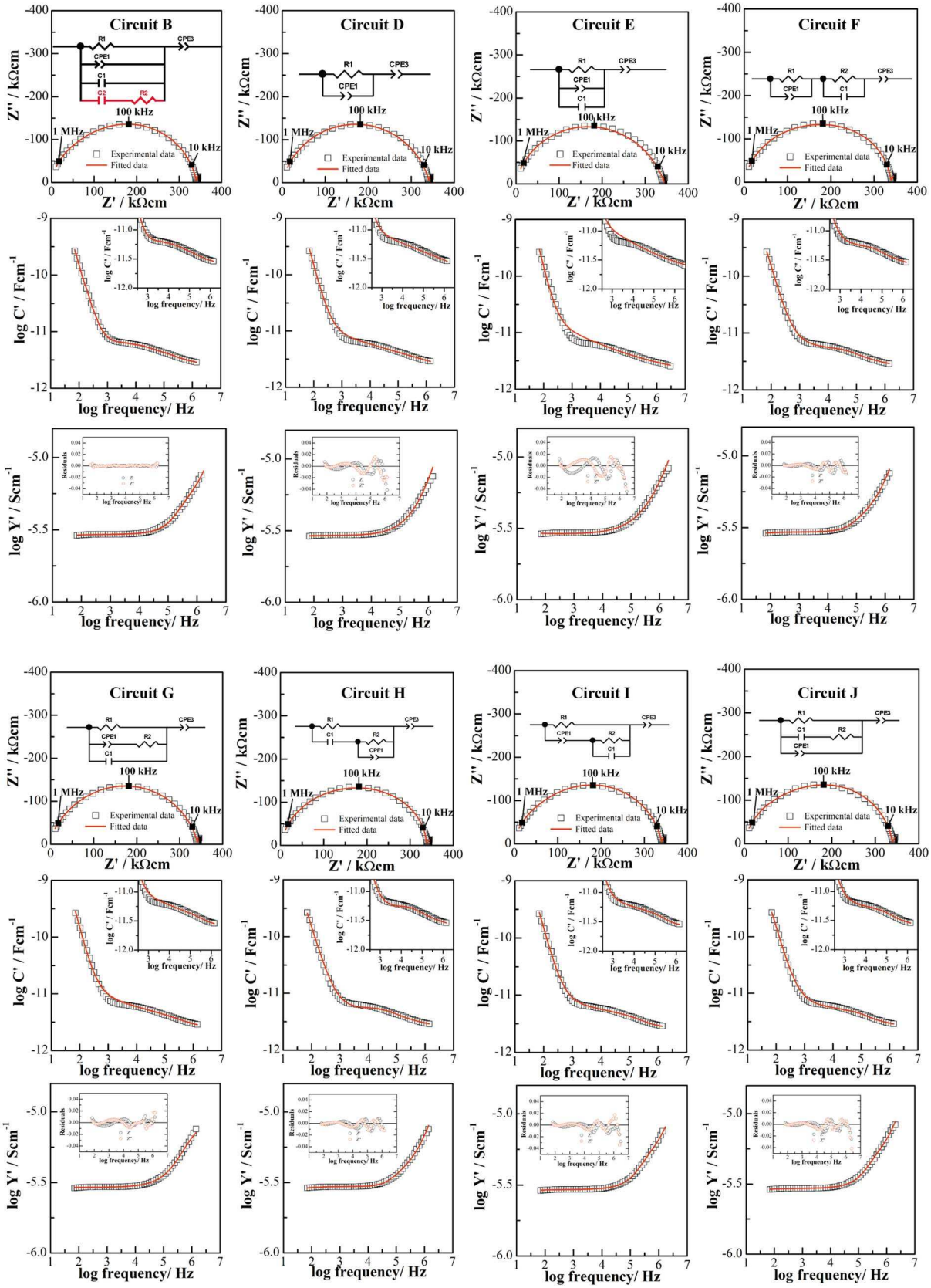

Figure 5. Experimental impedance data and fits to eight possible equivalent circuits measured at 306°C; the frequencies of some data points are indicated.

Table I. Fitted parameters of the different circuits tested for impedance data collected at 306°C.

Circuit	R_1 (kΩcm)	R_2 (kΩcm)	A_1 ($pScm^{-1}rad^{-n}$)	n_1	C_1 ($pFcm^{-1}$)	C_2 ($pFcm^{-1}$)	A_3 ($\mu Scm^{-1}rad^{-n}$)	n_3
B	339.3(2)	816(9)	14.5(2)	0.778(2)	2.33(3)	0.67(8)	0.21(3)	0.728(7)
D	342.1(7)	–	6.7(3)	0.855(3)	–	–	0.04(2)	0.86(1)
E	344.8(7)	–	17(2)	0.789(6)	1.1(1)	–	0.02(3)	0.899(6)
F	312(1)	28(1)	4.7(2)	0.882(3)	11.9(5)	–	0.04(3)	0.912(5)
G	342.7(5)	158(7)	17(1)	0.766(9)	2.63(4)	–	0.05(2)	0.793(8)
H	337.2(5)	179(8)	39(3)	0.805(5)	5.56(5)	–	0.6(1)	0.657(7)
I	340.7(8)	24(1)	2.8(2)	0.898(4)	15.8(8)	–	0.05(3)	0.825(4)
J	339.1(6)	116(4)	2.2(4)	0.903(3)	1.16(2)	–	0.24(6)	0.726(7)

high temperature, without the need in either case for vacancy-complex dissociation.

In order to investigate the effect of heating to high temperatures and subsequent cooling rate on the conductivity, (110)-oriented YSZ single crystals were annealed in air at 1200°C for 90 minutes and cooled at different rates. Figure 9a shows the Arrhenius plots of the samples cooled at different rates. All three data sets show non-linear Arrhenius plots, but slight differences can be observed in both high temperature (b) and low temperature (c) ranges. At high temperature, the sample quenched in liquid N_2 shows slightly lower conductivity than the samples cooled at 10 and 0.5°C/min, which show similar conductivities. Conversely, at low temperature, the quenched sample shows higher conductivity values than the samples cooled at intermediate and low cooling rates.

The equivalent circuit analysis results reported above have enabled us to identify the most appropriate equivalent circuits to represent the experimental data sets. At lower temperatures where the bulk response of the crystals can be seen in the available frequency range, it is clear that the bulk response contains two components which are in parallel, rather than a series-connected circuit which is usually appropriate for ceramic materials consisting of grain and grain boundary components. Thus, as expected, there is no evidence of a component attributable to grain boundaries or, indeed, to a surface layer or crystal inhomogeneity. We are therefore now in a position to consider the possible mechanistic origins of the two parallel components, one of which represents long range conduction and the other which appears to represent local conduction or a dielectric relaxation process.

The traditional explanation of curvature in conductivity Arrhenius plots of YSZ ceramics and single crystals is the so-called 'dipole-trapping model', which invokes the trapping of mobile oxygen vacancies by the Y acceptor dopants. The trapping arises because the dipole components have charges of opposite sign, i.e. using Kröger-Vink notation, they are Y' and $V_o^{\bullet\bullet}$. At lower temperatures, an additional dissociation enthalpy is required to enable long range conduction of the oxygen vacancies and this gives rise to an activation energy which contains terms for both dipole dissociation and vacancy migration. At higher temperatures, above the region of curvature in the Arrhenius plots, it is presumed that a sufficient number of dipoles are dissociated and therefore, the observed lower activation energy contains only the vacancy migration term.

Our equivalent circuit B is at least partly consistent with this model; the series element R_2-C_2 represents hopping of oxygen vacancies within the dipoles and therefore, leads to dipole reorientation but not long range vacancy migration. The dipole reorientation is an *ac* process only but occurs at the same time as long range *dc* conduction; therefore, R_2 does not contribute to the total crystal resistance R_t (= R_1). From the difference in activation energies of σ_1 and σ_2, the value of ~0.2 eV may be assigned to the dissociation enthalpy. This value is similar to that reported in the literature[11–15] based on high and low temperature activation energies whereas here, both values are obtained from the same, low temperature, data sets.

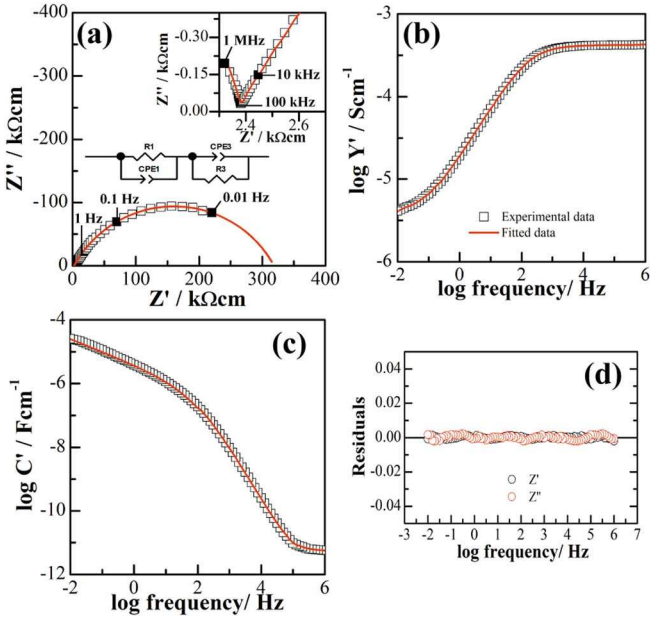

Figure 6. Impedance spectra for 8YSZ single crystal with the field perpendicular to (110) measured at 500°C. (a) Experimental and fitted data shown for impedance complex plane plot with the equivalent circuit used, (b) Y' spectroscopic plot, (c) C' spectroscopic plot and (d) residuals.

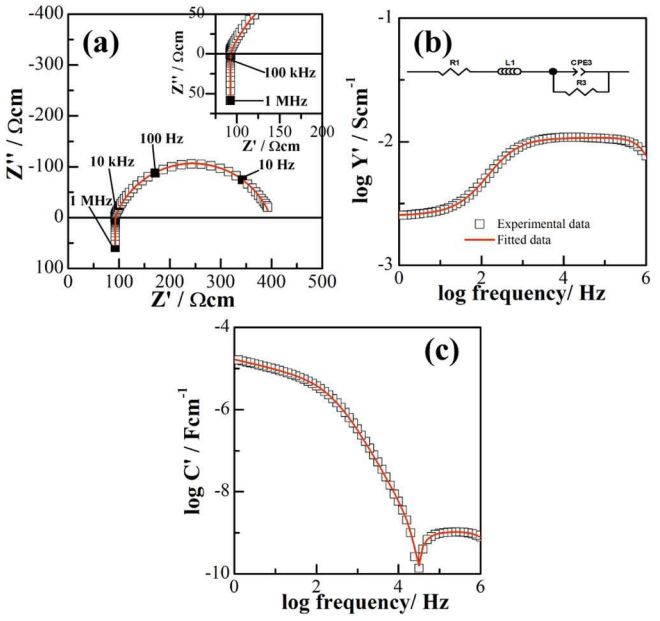

Figure 7. Impedance spectra for 8YSZ single crystal with the field perpendicular to (110) measured at 705°C. (a) Experimental and fitted data shown for impedance complex plane plot, (b) Y' spectroscopic plot with the equivalent circuit used, (c) C' spectroscopic plot.

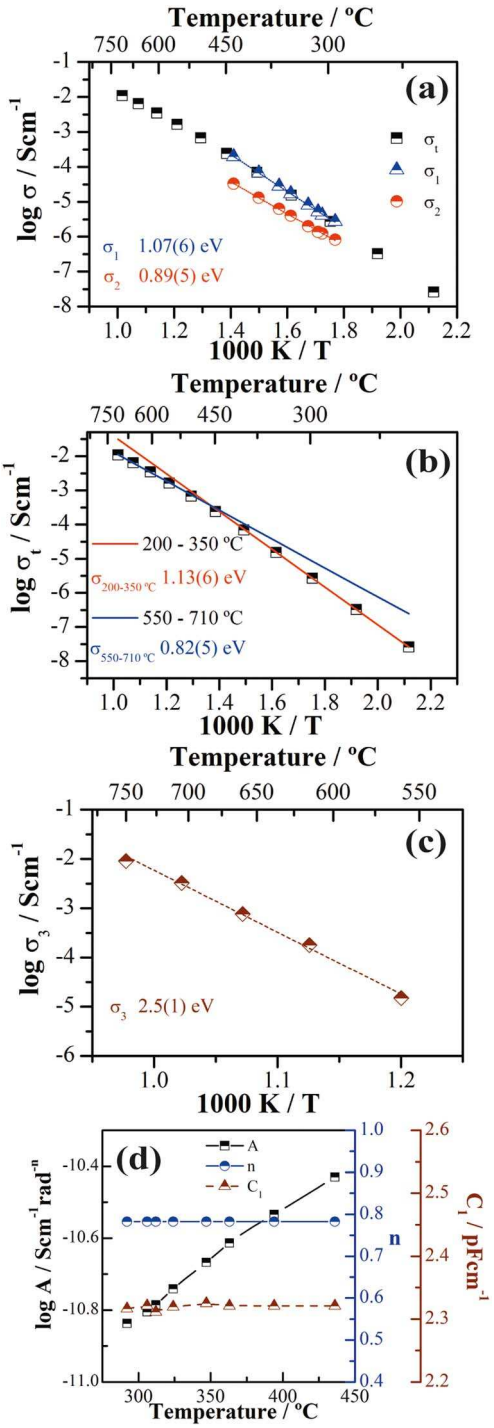

Figure 8. Arrhenius plots for (a) σ_t and for fitted values of σ_1 and σ_2, (b) for σ_t at low and high temperature, (c) R_3, and (d) fitted parameters A_1, n_1 of CPE_1 and C_1 for the (110) oriented 8YSZ single crystal.

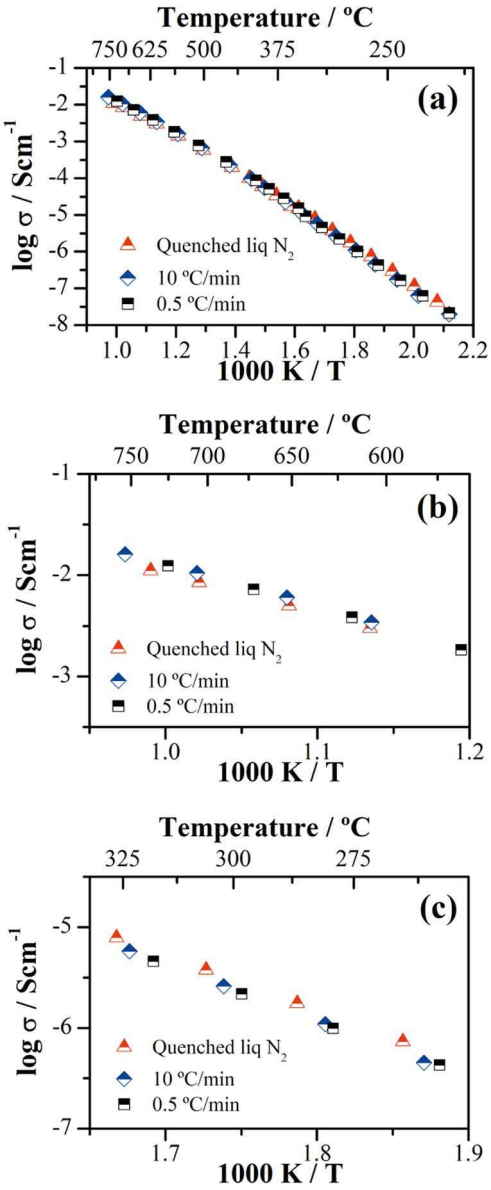

Figure 9. Arrhenius plots for (110)-oriented 8YSZ single crystals annealed in air at 1200°C and cooled at different rates (a) σ_t over the entire temperature range, (b) σ_t at high temperatures and (c) σ_t at low temperatures.

This simple dipole trapping model has certain drawbacks. As pointed out by Ahamer et al.,[15] these YSZ materials cannot be regarded as dilute defect systems since the dopant Y concentrations are far too high; it is difficult to imagine how genuinely-free oxygen vacancies could arise since there will always be Y dopants in the near vicinity of the oxygen vacancies. It is also difficult to explain the differences in conductivity observed between quenched and slow-cooled crystals using this model. As shown by Ahamer et al.[15] and also in Figure 9, quenched crystals have a higher conductivity at low temperatures followed by a slightly smaller conductivity at high temperatures. The increased conductivity at lower temperatures in the quenched samples could be interpreted reasonably as an increase in number of free oxygen vacancies arising from the dipole dissociation at high temperatures prior to quenching. However, the higher temperature data imply a reduction in mobile vacancy concentration which cannot be explained by a simple model of dipole dissociation.

Given the large concentration of both Y dopants and oxygen vacancies, other reversible structural changes may occur as a function of temperature which influence the mobile carrier concentration at high temperatures. High temperature neutron diffraction studies on YSZ powders showed additional broad diffuse scattering peaks which disappeared above 650°C and a discontinuity in thermal expansion coefficient data was used as evidence for the occurrence of a second order phase transition.[31]

We now consider the recently-proposed 'two different barrier heights' model[15] in which the conduction pathway involves a sequential combination of hops over two different barrier heights. This model can also account for curvature in the Arrhenius plots. Thus, at low temperatures the higher barrier limits the long range conductivity.

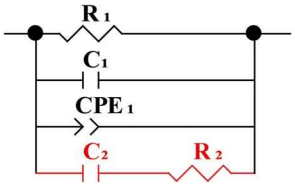

Figure 10. Equivalent circuit to model bulk long range and local conduction processes.

With increasing temperature, the higher barrier becomes less important since it has a higher activation energy than that for hops over the lower barriers. Consequently, at high temperatures, the lower barriers limit the long range conductivity.

A drawback of this model is that it is a series model and therefore, impedance data at low temperatures should fit an equivalent circuit that has two R, C components, representing the two barrier heights, which are placed in series. In addition, the spectrum of conductivity, Y'vs frequency should show two plateaux, one representing the overall conductivity at low frequencies and a second one at higher frequencies that includes the conductivity of the easier hops. In our impedance data, there is no evidence of a second series component in the equivalent circuit nor of two plateaux in the conductivity, Y', spectra. As with the dipole dissociation model, there is also the difficulty in explaining the differences in conductivity of quenched and slow-cooled samples.

In conclusion, there is a closer fit of the dipole model to the equivalent circuit B that contains two parallel conduction pathways, but the dipole model is a significant approximation to what must be complex, co-operative conduction mechanisms in which two activation barriers can be identified. Further, the nature of the defect clusters may change at a second order transition and involve more structural reorganization than simple dipole dissociation.

Crystallographic evidence for defect clusters has been obtained by single crystal neutron diffraction studies on YSZ crystals with a range of Y contents[32] and Sc-doped YSZ ceramics.[33,34] An important cluster appears to be a pair of oxygen vacancies, separated by a cation, in the $< 111 >$ direction. These are reported to be stable to high temperatures, close to melting. However, the precise nature of the structural changes to the defect complexes responsible for curvature in the Arrhenius plots is, at present, unknown. Possibly, two separate cluster formation mechanisms are involved; one involves $Y'_{Zr} - V_O^{\bullet\bullet}$ pairs and the other involves $V_O^{\bullet\bullet} - Zr - V_O^{\bullet\bullet}$ oxygen vacancy pairs. The increase in concentration of one kind of cluster may be at the expense of the second kind and this may be reflected in the conductivity data showing an enhanced conductivity at lower temperatures at the expense of a reduced conductivity at higher temperatures. However, this is speculation and requires further study.

Conclusions

Accurate representation of bulk impedance data of single crystal YSZ samples requires the presence of a dielectric element in the equivalent circuit in addition to the usual element that represents the bulk conductivity. The circuit that best fits the bulk response is a parallel combination of the R_1-C_1-CPE_1 conducting element with the R_2-C_2 dielectric element, Figure 10. R_1 represents the dc resistance of the sample and is the same as the total resistance R_t obtained by conventional complex plane analysis. R_2 represents the resistance to defect complex reorientation and has similar activation energy to the total resistance at high temperatures. We are, therefore, able to determine the parameters for local hopping or dipole reorientation separate from the long range, conductivity parameters.

Previous studies on YSZ ceramics showed the need for inclusion of the dipole element but a full assessment of the most appropriate circuit to represent the data was not made.[20] Here we show that, with single crystal data and no contribution from grain boundary impedances, it is possible to identify unambiguously the most appropriate equivalent circuit. Circuit B is also the most logical circuit since it represents the two parallel processes of conduction and dielectric relaxation.

Choice of the most appropriate equivalent circuit to fit and analyse data requires data presentation in numerous ways so as to give equal weighting to all impedance components over the entire frequency range. Conventional impedance complex plane plots on linear scales, $Z''vs\ Z'$, which have been widely used previously to analyse YSZ impedance data, are insensitive to impedance phenomena at high frequencies and were unable to discriminate between the various equivalent circuits that were considered and tested. It was found to be particularly useful to present impedance data as $\log Y'vs \log f$, which showed the distribution of conductivities and $\log C'vs \log f$, which showed the distribution of capacitances. These presentations were sensitive to additional impedance components because the equivalent circuit, Figure 10, has a parallel combination of contributing elements that are best separated using admittance-based formalisms and are an example of the truism: admittances add in parallel whereas impedances add in series.

As far as we are aware, the contribution of short range dielectric processes in parallel with long range ionic conduction has not been well-recognized previously in the analysis of impedance data of YSZ. However, the occurrence of series-based, local *ac* conduction processes as part of overall, long range *dc* conduction, is widely attributed to the frequency-dependent, power law *ac* conductivity at high frequencies, such as shown in Figures 1b, 3c, etc. Such processes are usually represented by a CPE, which can be deconvoluted into resistive and capacitive components, whose relative contribution is given by the CPE parameter, n. From present results, both CPE_1 and the dielectric processes, R_2-C_2, contribute to the overall impedance response of YSZ materials.

The activation energy for σ_2, which represents dipole reorientation, is similar to that of σ_t at high temperatures, where it is presumed that oxygen vacancies require no dissociation energy in order to move. The higher activation energy of σ_t at low temperatures therefore contains a contribution from dipole dissociation, estimated at ~0.2 eV. This simple model of dipole dissociation needs modification to take account of first, structural studies of defect complexes, including temperature-dependent cluster formation in diffuse scattering neutron diffraction data and second, the high concentration of dopants and oxygen vacancies which exceed greatly the limit for considerations using dilute defect equilibria.

These results on a single crystal sample show that the bulk response contains two components, representing dielectric and conduction processes. Recognition and modelling of this complexity may help to shed light on grain boundary contributions to the impedance of ceramic samples. The intermediate frequency capacitance plateau that we identify with the dielectric component C_2 has been in evidence in the impedance response of numerous other single crystal and ceramic samples,[35,36] not only of YSZ; it may therefore be a common feature of the impedance data of many ionic conductors.

Acknowledgments

This project has received funding from the European Union's Horizon 2020 research and innovation programme under the Marie Sklodowska-Curie grant agreement No 700786.

ORCID

Xavier Vendrell https://orcid.org/0000-0003-4705-8253
Anthony R. West https://orcid.org/0000-0002-5492-2102

References

1. A. Boudghene and E. Traversa, *Renew. Sustain. Energy Rev.*, **6**, 433 (2002).
2. V. Kharton, F. Marques, and A. Atkinson, *Solid State Ionics*, **174**, 135 (2004).
3. J. W. Fergus, *J. Power Sources*, **162**, 30 (2006).
4. E. J. Abram, D. C. Sinclair, and A. R. West, *J. Electroceramics*, **10**, 165 (2003).

5. B.-N. Kim et al., *J. Eur. Ceram. Soc.*, **36**, 1269 (2016).
6. C. Haering, A. Roosen, and H. Schichl, *Solid State Ionics*, **176**, 253 (2005).
7. J. Jiang, X. Hu, W. Shen, C. Ni, and J. L. Hertz, *Appl. Phys. Lett.*, **102**, 143901 (2013).
8. M. Mori et al., *Solid State Ionics*, **74**, 157 (1994).
9. S. P. S. Badwal, *J. Mater. Sci.*, **19**, 1767 (1984).
10. S. Kazlauskas, A. Kežionis, T. Šalkus, and A. F. Orliukas, *Solid State Ionics*, **231**, 37 (2013).
11. S. Ikeda, O. Sakurai, K. Uematsu, N. Mizutani, and M. Kato, *J. Mater. Sci.*, **20**, 4593 (1985).
12. P. S. Manning, J. D. Sirman, R. A. De Souza, and J. A. Kilner, *Solid State Ionics*, **100**, 1 (1997).
13. Y. Arachi, H. Sakai, O. Yamamoto, Y. Takeda, and N. Imanishai, *Solid State Ionics*, **121**, 133 (1999).
14. J. Luo, D. P. Almond, and R. Stevens, *J. Am. Ceram. Soc.*, **83**, 1703 (2000).
15. C. Ahamer, A. K. Opitz, G. M. Rupp, and J. Fleig, *J. Electrochem. Soc.*, **164**, F790 (2017).
16. J. S. Lee, U. Anselmi-Tamburini, Z. a. Munir, and S. Kim, *Electrochem. Solid-State Lett.*, **9**, J34 (2006).
17. J.-S. Lee and D.-Y. Kim, *J. Mater. Res.*, **16**, 2739 (2001).
18. I. M. Hodge, M. D. Ingram, and A. R. West, *J. Electroanal. Chem. Interfacial Electrochem.*, **74**, 125 (1976).
19. J. T. S. Irvine, D. C. Sinclair, and A. R. West, *Adv. Mater.*, **2**, 132 (1990).
20. M. A. Hernandez and A. R. West, *J. Mater. Chem. A*, **4**, 1298 (2016).
21. A. K. Jonscher, *Universal Relaxation Law*, p. 415, Chelsea Dielectrics Press, London, (1996).
22. D. P. Almond and B. Vainas, *J. Phys. Condens. Matter*, **11**, 9081 (1999).
23. D. P. Almond, C. R. Bowen, and D. A. S. Rees, *J. Phys. D. Appl. Phys.*, **39**, 1295 (2006).
24. P. Bruce, A. West, and D. Almond, *Solid State Ionics*, **7**, 57 (1982).
25. F. K. Moghadam and D. A. Stevenson, *J. Electrochem. Soc.*, **133**, 1329 (1986).
26. A. K. Jonscher, *J. Phys. D. Appl. Phys.*, **32**, R57 (1999).
27. M. A. Hernández, N. Masó, and A. R. West, *Appl. Phys. Lett.*, **108**, 152901 (2016).
28. S. Berendts, J. P. Eufinger, I. Valov, J. Janek, and M. Lerch, *Solid State Ionics*, **296**, 42 (2016).
29. T. Norby and M. Hartmonavá, *Solid State Ionics*, **67**, 57 (1993).
30. M. Kurumada, H. Hara, and E. Iguchi, *Acta Mater.*, **53**, 4839 (2005).
31. I. R. Gibson and J. T. S. Irvine, *J. Mater. Chem.*, **6**, 895 (1996).
32. J. Goff, W. Hayes, S. Hull, M. Hutchings, and K. Clausen, *Phys. Rev. B*, **59**, 14202 (1999).
33. S. T. Norberg et al., *Chem. Mater.*, **23**, 1356 (2011).
34. D. Marrocchelli, P. A. Madden, S. T. Norberg, and S. Hull, *Chem. Mater.*, **23**, 1365 (2011).
35. A. Pimenov, J. Ullrich, P. Lunkenheimer, A. Loidl, and C. H. Rüscher, *Solid State Ionics*, **109**, 111 (1998).
36. N. H. Perry, T. C. Yeh, and T. O. Mason, *J. Am. Ceram. Soc.*, **94**, 508 (2011).